

# Electronic Structure of Oxidized Complexes Derived from $cis\text{-}[\text{Ru}^{\text{II}}(\text{bpy})_2(\text{H}_2\text{O})_2]^{2+}$ and Its Photoisomerization Mechanism

Nora Planas,<sup>†</sup> Laura Vigarà,<sup>†</sup> Clyde Cady,<sup>‡</sup> Pere Miró,<sup>§</sup> Ping Huang,<sup>‡</sup> Leif Hammarström,<sup>‡</sup> Stenbjörn Styring,<sup>‡</sup> Nils Leidel,<sup>||</sup> Holger Dau,<sup>||</sup> Michael Haumann,<sup>||</sup> Laura Gagliardi,<sup>\*,§</sup> Christopher J. Cramer,<sup>\*,§</sup> and Antoni Llobet<sup>\*,†,⊥</sup>

<sup>†</sup>Institute of Chemical Research of Catalonia (ICIQ), Av. Països Catalans 16, E-43007 Tarragona, Spain

<sup>‡</sup>Department of Photochemistry and Molecular Science, Ångström Laboratory, Box 523, Uppsala University, SE-751 20 Uppsala, Sweden

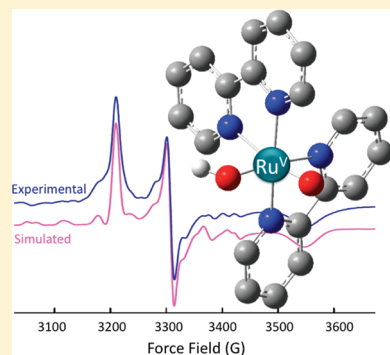
<sup>§</sup>Department of Chemistry and Supercomputing Institute, University of Minnesota, 207 Pleasant St. SE, Minneapolis, Minnesota 55455-0431, United States

<sup>||</sup>Department of Physics, Free University Berlin, D-14195 Berlin, Germany

<sup>⊥</sup>Departament de Química, Universitat Autònoma de Barcelona, Cerdanyola del Vallès, E-08193 Barcelona, Spain

**S** Supporting Information

**ABSTRACT:** The geometry and electronic structure of  $cis\text{-}[\text{Ru}^{\text{II}}(\text{bpy})_2(\text{H}_2\text{O})_2]^{2+}$  and its higher oxidation state species up formally to  $\text{Ru}^{\text{VI}}$  have been studied by means of UV–vis, EPR, XAS, and DFT and CASSCF/CASPT2 calculations. DFT calculations of the molecular structures of these species show that, as the oxidation state increases, the Ru–O bond distance decreases, indicating increased degrees of Ru–O multiple bonding. In addition, the O–Ru–O valence bond angle increases as the oxidation state increases. EPR spectroscopy and quantum chemical calculations indicate that low-spin configurations are favored for all oxidation states. Thus,  $cis\text{-}[\text{Ru}^{\text{IV}}(\text{bpy})_2(\text{OH})_2]^{2+}$  ( $d^4$ ) has a singlet ground state and is EPR-silent at low temperatures, while  $cis\text{-}[\text{Ru}^{\text{V}}(\text{bpy})_2(\text{O})(\text{OH})]^{2+}$  ( $d^3$ ) has a doublet ground state. XAS spectroscopy of higher oxidation state species and DFT calculations further illuminate the electronic structures of these complexes, particularly with respect to the covalent character of the O–Ru–O fragment. In addition, the photochemical isomerization of  $cis\text{-}[\text{Ru}^{\text{II}}(\text{bpy})_2(\text{H}_2\text{O})_2]^{2+}$  to its  $trans\text{-}[\text{Ru}^{\text{II}}(\text{bpy})_2(\text{H}_2\text{O})_2]^{2+}$  isomer has been fully characterized through quantum chemical calculations. The excited-state process is predicted to involve decoordination of one aqua ligand, which leads to a coordinatively unsaturated complex that undergoes structural rearrangement followed by recoordination of water to yield the *trans* isomer.



## 1. INTRODUCTION

Ruthenium complexes are of interest in a wide variety of fields, including photophysics, photochemistry,<sup>1,2</sup> bioninorganic chemistry,<sup>3</sup> and catalysis.<sup>4</sup> In the last instance, Ru–O groups play major roles in many redox catalytic processes, including the oxidation of water to dioxygen that is critical to the development of new, sustainable energy conversion schemes.<sup>5</sup> Many Ru complexes capable of oxidizing water to molecular oxygen have been reported in the literature.<sup>6–8</sup> The catalytic cycles for the various complexes share a common feature, namely, the intermediacy of ruthenium–oxo species in which the metal center is in a high formal oxidation state.

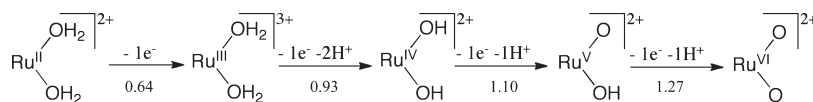
While the electronic structures of less oxidized species like  $\text{Ru}^{\text{II}}\text{--O}$  or  $\text{Ru}^{\text{III}}\text{--O}$  are well understood, equivalent details on the higher oxidation states  $\text{Ru}^{\text{IV}}\text{--O}$ ,  $\text{Ru}^{\text{V}}\text{--O}$ , and  $\text{Ru}^{\text{VI}}\text{--O}$  are scarce, in spite of their critical importance in catalytic processes.<sup>9</sup> The higher oxidation states are difficult to characterize, in part owing to their high reactivity. However, accurate structural and

electronic characterization of these states is critical for the evaluation of the degree of oxidation of the oxygen atoms in the various Ru–O groups and also for the assessment of the covalency of the Ru–O bond. Similar efforts to characterize highly oxidized intermediates have yielded detailed data for first row transition metal analogs like Cr, Mn, or Fe.<sup>10</sup>

In this work, we focus on the characterization of complexes derived from the oxidation of  $cis\text{-}[\text{Ru}^{\text{II}}(\text{bpy})_2(\text{H}_2\text{O})_2]^{2+}$  (bpy = 2,2′-bipyridine), hereafter referred to as  $cis\text{-}[\text{Ru}^{\text{II}}(\text{H}_2\text{O})_2]^{2+}$ , given the capacity of its  $\text{Ru}^{\text{VI}}$  oxidation state to oxidize water to dioxygen catalytically.<sup>11</sup> We employ UV–vis, electron paramagnetic resonance (EPR), and X-ray absorption (XAS) spectroscopies, and we apply density functional theory (DFT) and multiconfigurational complete active space self-consistent field theory (CASSCF) followed by second-order perturbation theory

**Received:** August 3, 2011

**Published:** October 12, 2011

Scheme 1. Electron-Transfer (ET) and Proton-Coupled Electron-Transfer (PCET) Reactions for  $cis\text{-}[\text{Ru}^{\text{II}}(\text{H}_2\text{O})_2]^{2+}$ <sup>a</sup>

<sup>a</sup> The  $E^{\text{O}}$  redox potentials at pH = 1.0 vs. SSCE are indicated below the arrow in V.

Table 1. Selected Bond Distances (Å) and Valence and Dihedral Angles (deg) for  $cis\text{-}$  and  $trans\text{-}[\text{Ru}^{\text{II}}(\text{H}_2\text{O})_2]^{2+}$  and Corresponding Oxidized Derivatives in the Gas Phase (See Figure 1 for Atom Labeling)

complex	ox. state	Ru–O1	Ru–O2	Ru–N1	Ru–N2	Ru–N3	Ru–N4	O1–Ru–O2	N1–N2/N3–N4 <sup>a</sup>
$cis\text{-}[\text{Ru}^{\text{II}}(\text{OH}_2)_2]^{2+}$	II	2.226 <sup>b</sup> (2.151)	2.226 (2.147)	2.024 (2.005)	2.075 (2.070)	2.075 (2.053)	2.024 (2.001)	82.9 (86.7)	91.5 (92.1)
$cis\text{-}[\text{Ru}^{\text{III}}(\text{OH}_2)_2]^{3+}$	III	2.176	2.201	2.027	2.095	2.094	2.031	83.5	87.5
$cis\text{-}[\text{Ru}^{\text{IV}}(\text{OH})_2]^{2+}$	IV	1.869	1.869	2.121	2.093	2.093	2.121	110.8	76.8
$cis\text{-}[\text{Ru}^{\text{V}}(\text{O})(\text{OH})]^{2+}$	V	1.696	1.881	2.138	2.086	2.123	2.204	111.2	79.2
$cis\text{-}[\text{Ru}^{\text{VI}}(\text{O})_2]^{2+}$	VI	1.688	1.688	2.218	2.115	2.114	2.218	124.5	75.0
$trans\text{-}[\text{Ru}^{\text{II}}(\text{OH}_2)_2]^{2+}$	II	2.165 (2.105)	2.166 (2.105)	2.129 (2.074)	2.083 (2.074)	2.131 (2.073)	2.082 (2.074)	176.4 (180.0)	154.9 180.0
$trans\text{-}[\text{Ru}^{\text{III}}(\text{OH}_2)_2]^{3+}$	III	2.081 (2.008)	2.081 (2.006)	2.123 (2.099)	2.110 (2.090)	2.122 (2.099)	2.110 (2.090)	175.0 (178.4)	154.5 (156.5)
$trans\text{-}[\text{Ru}^{\text{IV}}(\text{O})(\text{H}_2\text{O})]^{2+}$	IV	1.738	2.305	2.120	2.124	2.116	2.133	178.3	153.1
$trans\text{-}[\text{Ru}^{\text{V}}(\text{O})(\text{OH})]^{2+}$	V	1.922	1.715	2.127	2.126	2.148	2.125	177.8	154.1
$trans\text{-}[\text{Ru}^{\text{VI}}(\text{O})_2]^{2+}$	VI	1.713	1.713	2.151	2.151	2.151	2.151	180.0	155.9

<sup>a</sup> Dihedral angle between the planes defined by the Ru and N atoms of the two *bpy* ligands. <sup>b</sup> Optimized M06-L data; single-crystal X-ray data are provided in parentheses for  $cis\text{-}[\text{Ru}^{\text{II}}(\text{OH}_2)_2]^{2+}$ ,<sup>34</sup>  $trans\text{-}[\text{Ru}^{\text{II}}(\text{OH}_2)_2]^{2+}$ ,<sup>35</sup> and  $trans\text{-}[\text{Ru}^{\text{III}}(\text{OH}_2)_2]^{3+}$ .<sup>11b</sup>

(CASPT2).<sup>12</sup> We further analyze the photoisomerization of  $cis\text{-}[\text{Ru}^{\text{II}}(\text{H}_2\text{O})_2]^{2+}$  to  $trans\text{-}[\text{Ru}^{\text{II}}(\text{H}_2\text{O})_2]^{2+}$  at the DFT and time-dependent (TD) DFT levels of theory.<sup>13</sup>

## 2. EXPERIMENTAL SECTION

**Materials.** All reagents were obtained from Aldrich Chemical Co. in the highest purity commercially available and were used as received. High-purity deionized water was obtained by passing distilled water through a nanopure Mili-Q water purification system. Complex  $[\text{Ru}(\text{bpy})_2(\text{CO}_3)]$  was prepared following literature procedures.<sup>14</sup>

**Instrumentation and Measurements.** Higher oxidation states of  $cis\text{-}[\text{Ru}^{\text{II}}(\text{H}_2\text{O})_2]^{2+}$  or  $trans\text{-}[\text{Ru}^{\text{II}}(\text{H}_2\text{O})_2]^{2+}$  were generated by the corresponding addition of a 3.0 mM solution of  $(\text{NH}_4)_2[\text{Ce}(\text{NO}_3)_6]$  ( $\text{Ce}^{\text{IV}}$ ) in 0.1 M aqueous  $\text{CF}_3\text{SO}_3\text{H}$  at pH = 1.0 to a 0.1 mM solution of  $cis\text{-}[\text{Ru}^{\text{II}}(\text{H}_2\text{O})_2]^{2+}$  or  $trans\text{-}[\text{Ru}^{\text{II}}(\text{H}_2\text{O})_2]^{2+}$ , respectively, in the same media.

**UV–Vis Spectroscopy.** The spectra were recorded at 25 °C in a 1.0-cm-path length quartz cell on a VARIAN CARY 50-Bio.

**Electron Paramagnetic Resonance.** EPR spectra were recorded on a Bruker ELEXYS-E500 spectrometer equipped with a super-EPR049 microwave bridge and an SHQ4122 rectangular resonator. A low temperature was reached by using an Oxford 900 liquid helium cryostat and an ITC-503 temperature controller. EPR parameters: microwave frequency, 9.27 GHz; modulation frequency, 100 kHz; modulation amplitude, 10 G; temperature, 6 K; microwave power 2.0 mW. EPR simulation was performed using the Bruker XSophe-Xepr View software suit (v.1.1.4). A spin Hamiltonian having the form  $\hat{H} = \mu_B \hat{B} \hat{g} \hat{S} + \hat{S} \hat{A} \hat{I}$  was used for analysis, where spin-nuclear hyperfine coupling was introduced in addition to the Zeeman term. The  $g$  and  $A$  tensors were calculated using a matrix diagonalization method. The simulated spectrum was obtained after iterative optimization. Samples were prepared in the same manner as for UV–vis spectra, transferred to an EPR tube, and immediately frozen in liquid nitrogen.

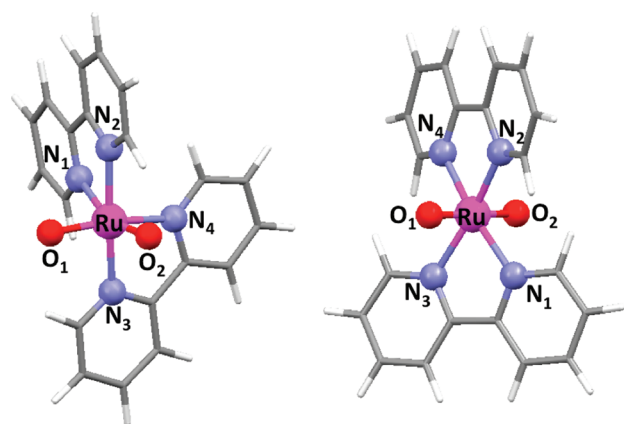
**X-Ray Absorption Spectroscopy (XAS).** XAS at the ruthenium K edge was performed at the SuperXAS beamline at Swiss Light Source (SLS at Paul Scherrer Institute, Villigen, Switzerland) with the storage ring operated in top-up mode.  $K_\alpha$ -fluorescence-detected XAS spectra were measured with an energy-resolving 13-element Ge detector (Canberra, shielded by a 25- $\mu\text{m}$ -thick Mo foil against scattered incident X-rays) on samples held in Teflon holders in a liquid-helium cryostat (Oxford) at 20 K, using excitation by X-rays from a double-crystal (Si311) monochromator (scan range 21.95–22.75 keV). Harmonics rejection was achieved by a platinum-covered toroidal mirror in grazing incidence mode. The beam was shaped by slits to a spot size on the sample of about  $4 \times 0.5 \text{ mm}^2$ . Energy calibration of each scan was done using the peak at 22.117 keV in the first derivative of absorption spectra of a Ru–metal powder sample measured in parallel to the complexes. About 5–8 spectra of powder samples and 12–18 spectra of solution samples (one scan of  $\sim 20$  min duration per sample spot) were averaged and normalized, and EXAFS spectra were derived as described previously.<sup>15</sup> EXAFS simulations were carried out using the software SimX<sup>15</sup> and phase functions calculated with FEFF8.<sup>16</sup> The absence of X-ray-induced photoreduction of ruthenium in solution and powder samples was verified by measurements of XAS spectra on a single sample spot, which were identical after 1–3 scans. Samples were prepared as described in the Materials subsection, transferred into Teflon buckets, and immediately frozen in liquid nitrogen.

**Density Functional Theory Calculations.** All molecular geometries were fully optimized at the M06-L<sup>17</sup> level using MN-GFM,<sup>18</sup> a locally modified version of Gaussian 03.<sup>19</sup> The ECP28MWB contracted Stuttgart basis set  $[8s7p6d2f]6s5p3d2f$  and pseudopotential were used on Ru,<sup>20</sup> and the 6-31G(d)<sup>21</sup> basis set was used on all other atoms. Integral evaluation made use of the grid defined as “ultrafine” in the Gaussian suite, and an automatically generated density-fitting basis set was used within the resolution of the identity approximation for the evaluation of Coulomb integrals. The nature of all stationary points was

**Table 2.** Computed State-Energy Splittings and Isomerization Energies ( $H_0$ , kcal/mol) for *trans* and *cis* Isomers of Different Ruthenium Complexes

complex	oxidation state	ground state	lowest excited state	adiabatic state-energy splitting M06-L <sup>a</sup> (CASPT2 <sup>b</sup> )	cis–trans isomerization energy M06-L <sup>a</sup> (CASPT2 <sup>b</sup> )
<i>cis</i> -[Ru <sup>II</sup> (OH <sub>2</sub> ) <sub>2</sub> ] <sup>2+</sup>	II	S <sub>0</sub> ( <sup>1</sup> A)			15.6
<i>trans</i> -[Ru <sup>II</sup> (OH <sub>2</sub> ) <sub>2</sub> ] <sup>2+</sup>	II	S <sub>0</sub> ( <sup>1</sup> A)			
<i>cis</i> -[Ru <sup>III</sup> (OH <sub>2</sub> ) <sub>2</sub> ] <sup>3+</sup>	III	D <sub>0</sub> ( <sup>2</sup> A)	Q <sub>1</sub> ( <sup>4</sup> A)	27.2	13.3
<i>trans</i> -[Ru <sup>III</sup> (OH <sub>2</sub> ) <sub>2</sub> ] <sup>3+</sup>	III	D <sub>0</sub> ( <sup>2</sup> A)	Q <sub>1</sub> ( <sup>4</sup> A)	11.4	
<i>cis</i> -[Ru <sup>IV</sup> (OH) <sub>2</sub> ] <sup>2+</sup>	IV	S <sub>0</sub> ( <sup>1</sup> A)	T <sub>1</sub> ( <sup>3</sup> A)	2.8	9.2
<i>trans</i> -[Ru <sup>IV</sup> (OH <sub>2</sub> )(O)] <sup>2+</sup>	IV	T <sub>0</sub> ( <sup>3</sup> A)	S <sub>1</sub> ( <sup>1</sup> A)	14.3	
<i>cis</i> -[Ru <sup>V</sup> (OH)(O)] <sup>2+</sup>	V	D <sub>0</sub> ( <sup>2</sup> A)	Q <sub>1</sub> ( <sup>4</sup> A)	12.7	13.8
<i>trans</i> -[Ru <sup>V</sup> (OH)(O)] <sup>2+</sup>	V	D <sub>0</sub> ( <sup>2</sup> A)	Q <sub>1</sub> ( <sup>4</sup> A)	24.4	
<i>cis</i> -[Ru <sup>VI</sup> (O) <sub>2</sub> ] <sup>2+</sup>	VI	S <sub>0</sub> ( <sup>1</sup> A)	T <sub>1</sub> ( <sup>3</sup> A)	3.8 (3.0)	8.8 (4.8)
<i>trans</i> -[Ru <sup>VI</sup> (O) <sub>2</sub> ] <sup>2+</sup>	VI	S <sub>0</sub> ( <sup>1</sup> A)	T <sub>1</sub> ( <sup>3</sup> A)	34.7 (39.6)	

<sup>a</sup> M06-L energies include the zero-point vibrational energy ( $H_0$ ). <sup>b</sup> CASPT2 energies are electronic energies only, and not  $H_0$ .

**Figure 1.** DFT optimized structure for *cis*- (left) and *trans*-[Ru<sup>VI</sup>(bpy)<sub>2</sub>(O)<sub>2</sub>]<sup>2+</sup> (right). Color code: Ru, green; N, blue; O, red; C, gray; H, white.

verified by analytic computation of vibrational frequencies, which were also used for the computation of molecular partition functions and 298 K thermal contributions to free energies, following the usual rigid-rotator, harmonic-oscillator, ideal-gas approximation.

For DFT singlet states, restricted self-consistent field solutions were obtained first and then checked for restricted-to-unrestricted internal instabilities. When such instabilities were found, the Kohn–Sham (KS) wave functions were reoptimized with an unrestricted formalism. Spin purification was employed to eliminate energetic contributions from triplet-state spin contamination of the broken-spin-symmetry KS determinants. Thus, the spin-purified singlet state energy is computed using eq 1, in which the triplet energy is computed for the single-determinantal high-spin ( $S_z = 1$ ) configuration (at the UDFT level), and  $\langle S^2 \rangle$  and  $E_{S_z=0}$  are, respectively, the expectation value of the total spin operator applied to and the energy determined from the broken-symmetry KS determinant.<sup>22</sup>

$$E_{\text{singlet}} = \frac{2E_{(S_z)=0} - \langle S^2 \rangle E_{(S_z)=1}}{2 - \langle S^2 \rangle} \quad (1)$$

For *cis*-[Ru<sup>II</sup>(OH<sub>2</sub>)<sub>2</sub>]<sup>2+</sup>, *trans*-[Ru<sup>II</sup>(OH<sub>2</sub>)<sub>2</sub>]<sup>2+</sup>, and intermediate species associated with the isomerization of one to the other, free energies of aqueous solvation were computed using the SMD continuum solvation model<sup>23</sup> for gas-phase geometries. A 1 M standard state was used for all species in aqueous solution, except for water itself, for which a 55.6 M

standard state was employed. Thus, for all molecules but water, the free energy in solution is computed as the 1 atm gas-phase free energy, plus a 1 atm to 1 M standard-state concentration change of  $RT \ln(24.5)$ , or 1.90 kcal/mol, plus the 1 M to 1 M SMD aqueous solvation free energy. In the case of water, the 1 atm gas-phase free energy is summed with 1 atm to a 55.6 M concentration standard-state change of 4.3 kcal/mol and the experimental 1 M to 1 M solvation free energy,  $-6.3$  kcal/mol.<sup>24</sup> Nonequilibrium solvation was employed for vertical excitations, while equilibrium solvation was employed for all states at their optimized geometries.

Optimized geometries for electronically excited states were computed with TDDFT using Gaussian 09<sup>25</sup> and the M06-L functional. Gas-phase thermal contributions for excited states were assumed to be unchanged from S<sub>0</sub> species. Single-point calculations on the M06-L geometries (both ground and excited states) were performed with the hybrid M06-2X<sup>26</sup> functional in order to improve excited-state energies. Full references for the Gaussian 03 and 09 packages are included in the Supporting Information.

**Multiconfigurational Calculations.** CASSCF and CASPT2 calculations<sup>27</sup> were performed for the DFT-optimized geometries of both the S<sub>0</sub> and T<sub>1</sub> spin states of *cis*- and *trans*-[Ru<sup>VI</sup>(bpy)<sub>2</sub>(O)<sub>2</sub>]<sup>2+</sup> using the MOLCAS 7.5 program package.<sup>28</sup> Scalar relativistic effects were included by use of the Douglas–Kroll–Hess Hamiltonian to second order<sup>29</sup> and the relativistic all-electron ANO-RCC<sup>30</sup> basis sets using a triple- $\zeta$  quality (ANO-RCC-VTZP) [7s6p4d2f1g] contraction for Ru; a double- $\zeta$  quality (ANO-RCC-VDZP) [3s2p1d] contraction for O, C, and N; and the minimal [1s] ANO-RCC-MB basis set for H. Several CASSCF active spaces were tested; ultimately, the chosen active space was 14 electrons in 11 orbitals, corresponding to linear combinations of the 4d orbitals of Ru<sup>VI</sup> (two electrons) and the valence orbitals of both O atoms (12 electrons). Two virtual orbitals of the 13 orbitals that would be generated from all possible metal d and oxygen valence orbitals had occupation numbers so near to zero that they were eliminated from the active space in production runs. All systems were found to be essentially single-configurational.

### 3. RESULTS AND DISCUSSION

The mononuclear complexes *cis*- and *trans*-[Ru<sup>II</sup>(H<sub>2</sub>O)<sub>2</sub>]<sup>2+</sup> were reported by Meyer et al. in 1988<sup>11b</sup> and were characterized thoroughly by UV–vis spectroscopy and electrochemical measurement of their corresponding Pourbaix diagrams, which provided full thermodynamic characterizations for the two complexes and the various species derived from them by e<sup>−</sup> and/or H<sup>+</sup> transfers. For *cis*-[Ru<sup>II</sup>(H<sub>2</sub>O)<sub>2</sub>]<sup>2+</sup> at pH = 1.0, a series of

Scheme 2. Orbital Interactions between the Ru 4d Orbitals and the O 2p Orbitals

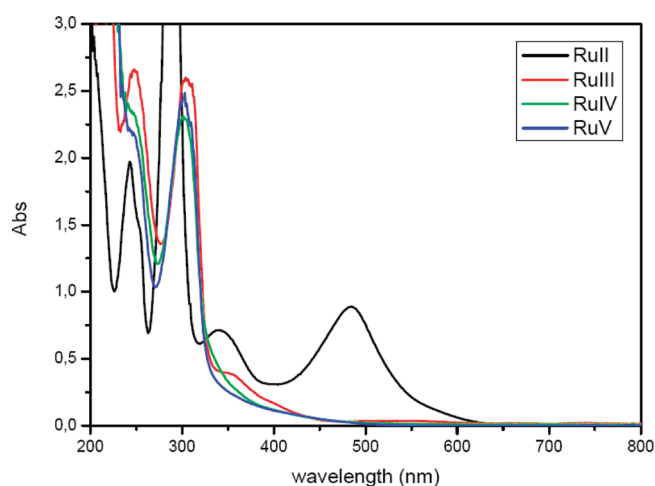
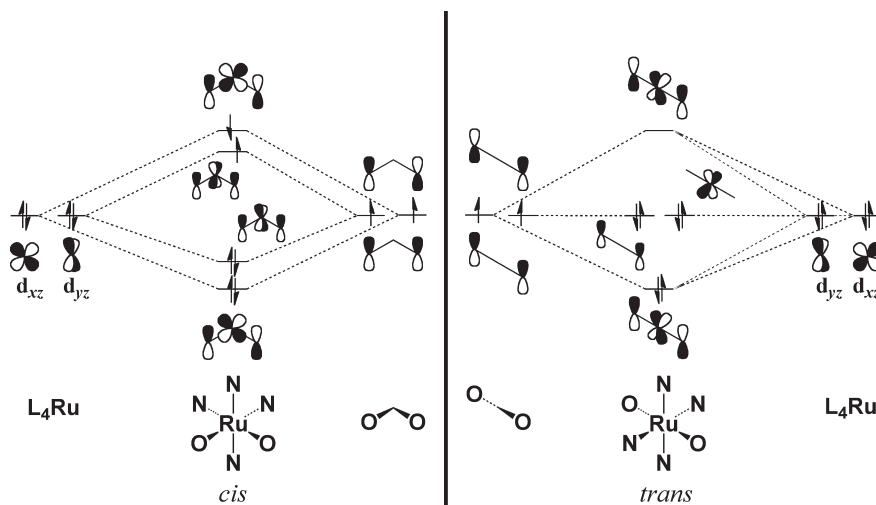


**Figure 2.** UV-vis spectra for  $\text{cis-}[\text{Ru}^{\text{II}}(\text{H}_2\text{O})_2]^{2+}$  (0.1 mM) at pH = 1.0 triflic acid aqueous solution and its corresponding higher oxidation state species at the same pH.

consecutive electron-transfer (ET) and proton-coupled electron-transfer (PCET) reactions occur upon oxidation, as shown in Scheme 1 (with *bpy* ligands omitted for clarity).

We have recently shown that upon the addition of a strong oxidant such as Ce(IV),  $\text{cis-}[\text{Ru}^{\text{II}}(\text{H}_2\text{O})_2]^{2+}$  acts as a water oxidation catalyst at pH = 1.0 in triflic acid solution.<sup>11a</sup> It is therefore at this pH that we have carried out all of the experiments described herein. It is interesting to note here that in the absence of light the  $\text{cis-}[\text{Ru}^{\text{II}}(\text{H}_2\text{O})_2]^{2+}$  complex is stable but in the presence of light it undergoes  $\text{cis} \rightarrow \text{trans}$  isomerization, since in the photostationary state the *trans* isomer is slightly favored.<sup>36</sup> Another point of further interest is the much lower activity of the  $\text{trans-}[\text{Ru}^{\text{II}}(\text{H}_2\text{O})_2]^{2+}$  analogue for water oxidation. This implies that no significant isomerization is taking place in the water oxidation process catalyzed by the  $\text{cis-}[\text{Ru}^{\text{II}}(\text{H}_2\text{O})_2]^{2+}$  complex.<sup>11a</sup>

**Geometries and Electronic Structures.** DFT geometry optimizations of the *cis*- and *trans*- $[\text{Ru}^{\text{II}}(\text{H}_2\text{O})_2]^{2+}$  species and their more highly oxidized derivatives shown in Scheme 1 were accomplished at the M06-L level. Selected bond distances and

valence bond angles for the lowest energy *cis* and *trans* isomers of differently oxidized ground-state species, as well as single-crystal X-ray data where available, are presented in Table 1; state-energy splittings and isomerization energies are presented in Table 2. For the intermediate with formal oxidation state IV, two possible species,  $[\text{Ru}^{\text{IV}}(\text{OH})_2]^{2+}$  and  $[\text{Ru}^{\text{IV}}(\text{OH}_2)(\text{O})]^{2+}$ , were identified for each stereoisomer. For the *cis* isomer, the dihydroxy tautomer is more stable than the aquo/oxo tautomer by 0.6 kcal/mol, while for the *trans* isomer this stability order is reversed with a preference of 1.4 kcal/mol; metric data for the higher energy tautomers are in Table S1 of the Supporting Information.

Noteworthy bond-length trends in Table 1 include that, in low oxidation states, Ru–OH<sub>2</sub> distances are significantly *shorter* for *trans* isomers than for *cis* analogs (see also, Figure 1). In high oxidation states, by contrast, the Ru=O/Ru–OH distances are slightly *longer* for *trans* isomers than for *cis* analogs. Irrespective of the isomer, a substantial decrease in Ru–O bond lengths is observed with increasing oxidation, suggestive of increased Ru–O bond order. This trend is consistent with that observed with the experimental Ru–O distances for  $[\text{Ru}^{\text{IV}}(\text{O})(\text{damp})(\text{bpy})]^{2+}$  (1.805 Å; damp is 2,6-bis((dimethylamino)methyl)pyridine),<sup>31</sup>  $\text{trans-}[\text{Ru}^{\text{VI}}(15\text{-TMC})(\text{O})_2]$  (1.718 Å; 15-TMC is 1,4,8,12-tetramethyl-1,4,8,12-tetraazapentadecane),<sup>32</sup> and  $t,t,t\text{-}[\text{Ru}^{\text{VI}}(\text{O})_2\text{-(py)}_2(\text{OAc})_2]$  (1.726 Å).<sup>33</sup> Last, a significant *trans* effect causes the Ru–N(*bpy*) bonds *trans* to the Ru–O bonds (thus, N2 and N3) in  $\text{cis-}[\text{Ru}^{\text{IV}}(\text{OH})_2]^{2+}$  to be longer than those Ru–N(*bpy*) bonds that are *trans* to one another (N1 and N4).

With respect to valence bond angles in the *cis*-Ru complexes, the O–Ru–O angle progressively increases from 83° in oxidation state II to 124° in oxidation state VI. This large angle at the highest oxidation state is consistent with repulsive oxygen lone pair interactions that contribute to an unfavorable intramolecular O–O bond formation pathway found for this species, as elucidated by prior <sup>18</sup>O labeling experiments and DFT and CASPT2 studies.<sup>11a</sup>

Turning to questions of electronic structure, all of the molecules in Tables 1 and 2 have ground states characterized by maximum spin pairing, i.e., singlet or doublet ground states for even and odd numbers of electrons, respectively, except that a triplet ground state is computed for  $\text{trans-}[\text{Ru}^{\text{IV}}(\text{OH}_2)(\text{O})]^{2+}$ . The analogous  $\text{cis-}[\text{Ru}^{\text{IV}}(\text{OH}_2)(\text{O})]^{2+}$  (with geometric data in



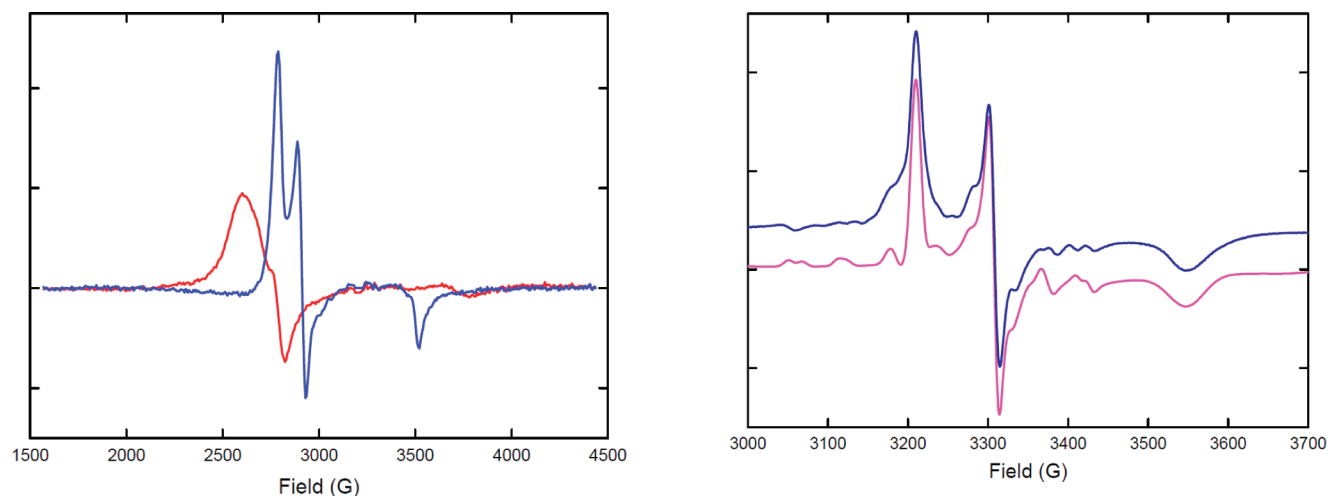


**Figure 3.** Left, EPR spectra of complexes  $cis\text{-}[\text{Ru}^{\text{III}}(\text{H}_2\text{O})_2]^{3+}$  (red) and  $trans\text{-}[\text{Ru}^{\text{III}}(\text{H}_2\text{O})_2]^{3+}$  (blue). Right, experimental (dark blue) and simulated (pink) EPR spectra of complex  $cis\text{-}[\text{Ru}^{\text{V}}(\text{O})(\text{OH})]^{2+}$ .

Table S1, Supporting Information) also has a triplet ground state, consistent with prior work, suggesting that formal  $\text{Ru}^{\text{IV}}=\text{O}^{2-}$  mono-oxo ruthenium species may be better represented as triplet coupled  $\text{Ru}^{\text{III}}-\text{O}^{\bullet-}$  fragments.<sup>9a</sup>

In most cases, the state-energy splittings for corresponding *cis* and *trans* complexes are significantly different in magnitude. The most significant example is  $[\text{Ru}^{\text{VI}}(\text{O})_2]^{2+}$ , where the singlet–triplet splitting is predicted to be more than 30 kcal/mol larger for the *trans* isomer than the *cis*. This trend can be understood from consideration of hybrid interactions between the Ru 4d orbitals and the O 2p orbitals for these different geometries, as illustrated in Scheme 2. Sala et al.<sup>11a</sup> have already noted the near degeneracy of the frontier orbitals in the *cis* isomer (left side of Scheme 2) that leads to the small singlet–triplet splitting. However, in the *trans* isomer (right side of Scheme 2), only one of the Ru 4d orbitals remains capable of interacting with the O 2p orbitals, leading to a very strong preference to spin-pair the electrons in the now nonbonding d orbital and leaving a large frontier-orbital separation. This same orbital interaction affects less oxidized species, although proton attachments to oxygen diminish the contributions of O 2p orbitals to molecular hybrid orbitals.

Table 2 further indicates that for all oxidation states, *cis* compounds are more stable than their corresponding *trans* isomers. For  $[\text{Ru}^{\text{II}}(\text{OH})_2]^{2+}$  itself, this equilibrium preference has been established experimentally.<sup>36</sup>

**UV–Vis and EPR Spectroscopy.** The UV–vis spectra of complexes  $cis\text{-}[\text{Ru}^{\text{II}}(\text{H}_2\text{O})_2]^{2+}$ ,  $cis\text{-}[\text{Ru}^{\text{III}}(\text{H}_2\text{O})_2]^{3+}$ ,  $cis\text{-}[\text{Ru}^{\text{IV}}(\text{OH})_2]^{2+}$ , and  $cis\text{-}[\text{Ru}^{\text{V}}(\text{O})(\text{OH})]^{2+}$  are reported in Figure 2. All of the species were generated in situ by adding equivalent amounts of  $\text{Ce}^{\text{IV}}$ , in the absence of light so as to avoid the *cis*→*trans* isomerization reaction. For  $cis\text{-}[\text{Ru}^{\text{II}}(\text{H}_2\text{O})_2]^{2+}$ , the spectrum includes a region below 300 nm where bpy-based  $\pi\text{--}\pi^*$  transitions are observed and one above 300 nm where MLCT and  $d\text{--}d$  bands occur. For oxidation state II, the *cis* isomer presents two MLCT bands centered at 350 and 490 nm and a shoulder at 575 nm that can be assigned to a  $d\text{--}d$  band. Upon oxidation to formal  $\text{Ru}^{\text{III}}$ , the spectrum changes significantly: the MLCT band at 490 disappears, and two low intensity bands are observed at 350 and 550 nm. Additional oxidation to formal states IV and V results in spectra lacking MLCT and  $d\text{--}d$  bands above 350 nm.

The EPR spectra of complexes  $cis\text{-}[\text{Ru}^{\text{III}}(\text{H}_2\text{O})_2]^{3+}$ ,  $trans\text{-}[\text{Ru}^{\text{III}}(\text{H}_2\text{O})_2]^{3+}$ , and  $cis\text{-}[\text{Ru}^{\text{V}}(\text{O})(\text{OH})]^{2+}$  are depicted in Figure 3. The complexes  $cis\text{-}[\text{Ru}^{\text{II}}(\text{H}_2\text{O})_2]^{2+}$  and  $cis\text{-}[\text{Ru}^{\text{IV}}(\text{OH})_2]^{2+}$  were EPR-silent, indicating that the Ru center in both complexes is in the low-spin configuration, resulting in a diamagnetic ground state in both cases. This ground-state assignment agrees with the DFT predictions presented above.

The EPR spectra of complexes  $cis\text{-}[\text{Ru}^{\text{III}}(\text{H}_2\text{O})_2]^{3+}$  and  $trans\text{-}[\text{Ru}^{\text{III}}(\text{H}_2\text{O})_2]^{3+}$  (Figure 3, left) show spectral features characteristic for a spin  $S = 1/2$  in a rhombic environment, indicating that also in this oxidation state, the low-spin configuration is the most stable, in agreement with DFT. The anisotropic  $g$  values, arbitrarily denoted as  $g_1$ ,  $g_2$ , and  $g_3$ , for the  $cis\text{-}[\text{Ru}^{\text{III}}(\text{H}_2\text{O})_2]^{3+}$  complex are 2.55, 2.40, and 1.75, respectively; and for  $trans\text{-}[\text{Ru}^{\text{III}}(\text{H}_2\text{O})_2]^{3+}$ , they are 2.38, 2.27, and 1.88, respectively. These  $g$  values are consistent with previously described  $d^5$   $\text{Ru}(\text{III})$  complexes.<sup>37</sup> It is observed that the anisotropy (measured by the largest  $\Delta g$ ) in the *cis* conformation is 0.8, which is significantly larger than the corresponding value of 0.5 measured for the *trans* conformation. Moreover, the line width in the EPR spectrum of the  $cis\text{-}[\text{Ru}^{\text{III}}(\text{H}_2\text{O})_2]^{3+}$  complex is much broader than that in the spectrum for  $trans\text{-}[\text{Ru}^{\text{III}}(\text{H}_2\text{O})_2]^{3+}$ . The larger spin anisotropy and the broader line width in the *cis* form could be associated with different solvation-shell arrangements available to *cis* with regard to *trans*.

The EPR spectrum for the  $cis\text{-}[\text{Ru}^{\text{V}}(\text{O})(\text{OH})]^{2+}$  complex is also shown in Figure 3 (right, blue). In this complex, the  $\text{Ru}^{\text{V}}$  center is a  $d^3$  ion that can potentially adopt a low-spin ( $S = 1/2$ ) or high-spin ( $S = 3/2$ ) configuration. EPR simulations assuming either an  $S = 3/2$  or an  $S = 1/2$  ground state have been performed using the spin Hamiltonian  $\hat{H} = \mu_B \hat{B} g \hat{S} + \hat{S} \hat{A} \hat{I}$ , in order to determine the ground state spin. A very good agreement between the simulated and experimental spectra (Figure 3, right; pink and blue spectra, respectively) is obtained for  $S = 1/2$ , whereas no good simulation can be obtained for  $S = 3/2$ . The calculated EPR spectrum is obtained by using anisotropic EPR parameters  $g_x = 2.065$ ,  $g_y = 2.004$ ,  $g_z = 1.868$ ,  $A_x = 54.3$ ,  $A_y = 40.2$ , and  $A_z = 39.3 \times 10^{-4} \text{ cm}^{-1}$ . This  $S = 1/2$  ground state is in good agreement with DFT, which suggests that the low-spin (doublet) state is more stable by 14 kcal/mol than the high spin (quartet) state. Extensive

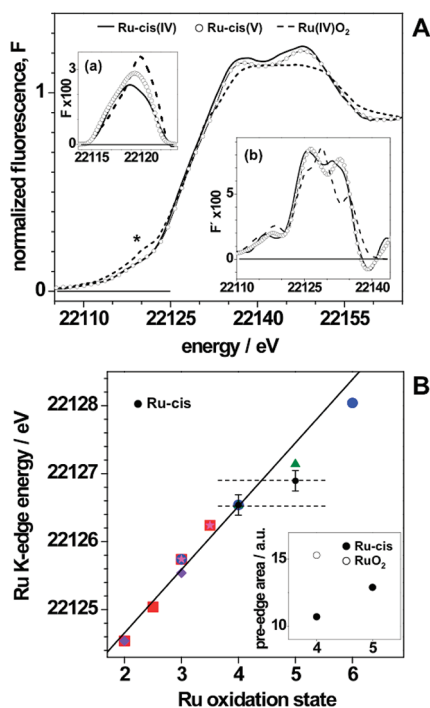


**Figure 4.** (A) Ruthenium K-edge spectra for  $cis\text{-}[\text{Ru}^{\text{IV}}(\text{OH})_2]^{2+}$  and  $cis\text{-}[\text{Ru}^{\text{V}}(\text{OH})(\text{O})]^{2+}$  and for  $\text{RuO}_2$  for comparison purposes. The asterisk (\*) denotes a pre-edge feature due to  $1s \rightarrow 4d$  electronic transitions. Inset a: extracted pre-edge peak features of spectra. Inset b: first derivatives of K-edge spectra. (B) K-edge energies for  $cis\text{-}[\text{Ru}^{\text{IV}}(\text{OH})_2]^{2+}$  and  $cis\text{-}[\text{Ru}^{\text{V}}(\text{OH})(\text{O})]^{2+}$  complexes (black circles) and literature data versus metal oxidation state. Horizontal dashes mark the edge energy difference between  $cis\text{-}[\text{Ru}^{\text{IV}}(\text{OH})_2]^{2+}$  and  $cis\text{-}[\text{Ru}^{\text{V}}(\text{OH})(\text{O})]^{2+}$ . K-edge energies correspond to values at 50% levels of edge rise. Literature values were derived from K-edge spectra of the following complexes:<sup>39</sup>  $[\text{Ru}_2(\mu\text{-O})(\mu\text{-CH}_3\text{COO})_2(\text{bpy})_2\text{L}_2]^{n+}$  (L = pyridine, 1-methylimidazol) in four oxidation states (red squares);<sup>39b</sup>  $\text{Ru}^{\text{III}}(\text{acac})_3$ ,  $\text{Ru}^{\text{IV}}\text{O}_2$ , and  $[\text{PW}_{11}\text{O}_{39}\text{-}\{\text{Ru}^{\text{VI}}\text{N}\}]$  (blue circles);<sup>39c</sup>  $\text{Sr}_2\text{Mn}_{0.5}\text{Ru}_{0.5}\text{O}_4$  and  $\text{Ru}^{\text{IV}}\text{O}_2$  (green triangles);<sup>39d</sup>  $[\text{Ru}^{\text{II}}\text{Cl}_2\text{LMe}_4]$  and  $[\text{Ru}^{\text{III}}\text{Cl}_4(\text{DMSO})_2]^-$  (violet diamonds);<sup>39d</sup> and  $[\text{Ru}^{\text{III}}(\text{bpy})_2(\text{H}_2\text{O})_2(\mu\text{-O})]^{4+}$  in two oxidation states (magenta stars).<sup>39a</sup> Data points were normalized to the value for  $cis\text{-}[\text{Ru}^{\text{IV}}(\text{OH})_2]^{2+}$  (solid circle). A regression line has been plotted for the complexes of Ru in oxidation states II, III, and IV that exhibits a slope of 1.04 eV per oxidation state. Inset: pre-edge peak areas for  $cis\text{-}[\text{Ru}^{\text{IV}}(\text{OH})_2]^{2+}$  and  $cis\text{-}[\text{Ru}^{\text{V}}(\text{OH})(\text{O})]^{2+}$  (solid circles) and  $\text{RuO}_2$  (open circle) derived from spectra in A.

EPR data are available in the literature for  $\text{Ru}^{\text{III}}$  complexes, but  $\text{Ru}^{\text{V}}$  examples are scarce. However, the  $g$  values we have obtained here for  $cis\text{-}[\text{Ru}^{\text{V}}(\text{O})(\text{OH})]^{2+}$  are relatively close to those determined for  $[\text{Ru}^{\text{V}}(\text{O})(\text{O}_2\text{COEt})_2](n\text{-Pr}_4\text{N})$  ( $g_x = 2.076$ ,  $g_y = 1.977$ ,  $g_z = 1.910$ )<sup>38</sup> and thus support equivalent oxidation states for these two compounds.

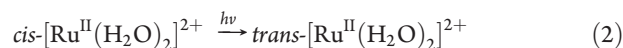
**XAS Spectroscopy.** XAS measurements were carried out to derive structural and electronic information for Ru–O-type complexes in their higher oxidation states. For this purpose, the complexes  $cis\text{-}[\text{Ru}^{\text{IV}}(\text{OH})_2]^{2+}$  and  $cis\text{-}[\text{Ru}^{\text{V}}(\text{O})(\text{OH})]^{2+}$  (1 mM) were prepared in aqueous solution containing 0.1 M triflic acid by adding two and three equivalents of  $\text{Ce}^{\text{IV}}$  to a solution of  $[\text{Ru}^{\text{II}}(\text{H}_2\text{O})_2]^{2+}$ , respectively. Figure 4A shows the X-ray absorption near-edge structure (XANES) spectra obtained for the  $cis\text{-}[\text{Ru}^{\text{IV}}(\text{OH})_2]^{2+}$  and  $cis\text{-}[\text{Ru}^{\text{V}}(\text{OH})(\text{O})]^{2+}$  complexes together with their first derivatives and isolated pre-edge features in

the insets. Figure 4B presents a graph of the Ru K-edge energies (at 50% level of spectra) versus Ru oxidation state for our complexes and representative literature<sup>39–41</sup> data and the respective pre-edge peak areas in the inset. The edge shapes of the  $cis\text{-}[\text{Ru}^{\text{IV}}(\text{OH})_2]^{2+}$  and  $cis\text{-}[\text{Ru}^{\text{V}}(\text{OH})(\text{O})]^{2+}$  complexes were rather similar, indicating that only minor structural changes in the first ruthenium coordination sphere occurred upon the oxidation.

Literature complexes show that when Ru is oxidized from II to IV the K-edge energies increase by close to 1.0 eV for each metal-centered oxidation step (Figure 4B). This notion takes into account the limited accuracy of the edge energy determination, which is on the order of  $\pm 0.15$  eV, and edge shape changes due to the various Ru coordination environments in the complexes, which slightly affect the apparent edge energy.<sup>40</sup> The smaller edge energy increase, in our case, of 0.35 eV (as shown in Figure 4B) upon going from formal  $\text{Ru}^{\text{IV}}$  to formal  $\text{Ru}^{\text{V}}$  can be interpreted in terms of shared oxidation of the Ru center and the oxygen atom. The partial oxidation of the oxygen can be rationalized in terms of a resonance such as  $\text{Ru}^{\text{V}}=\text{O}^{2-} \leftrightarrow \text{Ru}^{\text{IV}}-\text{O}^{\bullet-}$ . Interpreting the 0.35 eV increase quantitatively, this suggests that in  $cis\text{-}[\text{Ru}^{\text{V}}(\text{OH})(\text{O})]^{2+}$  there are roughly 65% and 35% weights of the oxyl and oxo forms, respectively. Additionally, the calculated Mulliken spin densities are 0.526 and 0.517 for Ru and O centers, respectively. These spin densities are consistent with substantial oxyl character. On the other hand, the pre-edge peak areas (Figure 4B) considerably increase from  $cis\text{-}[\text{Ru}^{\text{IV}}(\text{OH})_2]^{2+}$  to  $cis\text{-}[\text{Ru}^{\text{V}}(\text{OH})(\text{O})]^{2+}$  but are smaller than for  $\text{RuO}_2$ , indicating a significantly higher multiple bond character of the Ru–O bond in oxidation state V than in the IV. This is also in agreement with the DFT analysis where, upon increasing the oxidation state, the Ru–O bond distance is sharply reduced.

EXAFS analysis was carried out for the  $cis\text{-}[\text{Ru}^{\text{IV}}(\text{OH})_2]^{2+}$  and  $cis\text{-}[\text{Ru}^{\text{V}}(\text{OH})(\text{O})]^{2+}$  complexes (Figure 2A) to derive bond lengths in frozen solution samples. The EXAFS spectra were well simulated by the inclusion of N and O atoms for the first coordination sphere of Ru, together with a second sphere of closest C atoms (from the *bpy* ligands). The inclusion of longer interatomic distances did not alter the results for the first sphere (not shown). The determined bond lengths are reported in Table 3, and as expected the Ru–O distances decrease with oxidation state. In the  $cis\text{-}[\text{Ru}^{\text{IV}}(\text{OH})_2]^{2+}$  sample, simulations including a short Ru–O distance of  $\sim 1.7$  Å ascribable to a Ru=O bond resulted in almost no improvement in the fit quality (diminishing of the error sum,  $R_F$ , by an insignificant value of only 1%) and giving a coordination number close to zero for Ru=O. This indicates that the Ru=O species is not present in the  $cis\text{-}[\text{Ru}^{\text{IV}}(\text{OH})_2]^{2+}$  complex. For  $cis\text{-}[\text{Ru}^{\text{V}}(\text{OH})(\text{O})]^{2+}$ , on the other hand, a simulated value of  $\sim 1.7$  Å assigned for the Ru(V)=O bond, in good agreement with our DFT calculations reported above, leads to a substantially improved fit (Figure 5B).

**Isomerization of  $[\text{Ru}^{\text{II}}(\text{H}_2\text{O})_2]^{2+}$ .** In the presence of light, the predominant  $cis\text{-}[\text{Ru}^{\text{II}}(\text{H}_2\text{O})_2]^{2+}$  isomer is converted to the corresponding *trans* isomer, as shown in the eq 2.<sup>36</sup>



The analogous isomerization also occurs for the one-electron oxidized  $\text{Ru}^{\text{III}}$  species,<sup>35</sup> but no information is available for the corresponding higher oxidation state species. We have used TDDFT to explore the microscopic mechanism associated with eq 2 at the M06-2X//M06-L level of theory; energetic details are provided in Table 4 and Figure 6. M06-L is convenient for

**Table 3.** Ru–Ligand Distances for the *cis*-[Ru<sup>IV</sup>(OH)<sub>2</sub>]<sup>2+</sup> and *cis*-[Ru<sup>V</sup>(OH)(O)]<sup>2+</sup> Complexes from EXAFS Analysis

	fit	$n$ [per Ru]/ $R$ [Å]/ $2\sigma^2 \times 10^3$ [Å <sup>-1</sup> ] <sup>a,b</sup>				$R_F$ <sup>c</sup> (%)
		Ru=O	Ru–O	Ru–N	Ru–C	
<i>cis</i> -[Ru <sup>IV</sup> (OH) <sub>2</sub> ] <sup>2+</sup>	a		2/2.005/2	4/2.073/2	8/2.963/8	21.1
	b	0.11/ 1.698/2	1.89/ 2.005/2	4/2.072/2	8/2.963/8	20.1
<i>cis</i> -[Ru <sup>V</sup> (OH)(O)] <sup>2+</sup>	c		2/2.002/2	4/2.095/2	8/2.968/11	26.3
	d	0.36/ 1.710/2	1.64/ 2.046/2	4/2.074/6	8/2.972/10	22.2

<sup>a</sup>  $n$  is the number of atoms surrounding the metal center.  $R$  is the distance between the Ru atom and the atoms in the first and second coordination sphere.  $2\sigma^2$  is the Debye–Waller parameter. <sup>b</sup> All coordination numbers ( $n$ ) were fixed at their respective values in the crystal structure in the simulations except for simulations b and d, in which the  $n$ -values of the two Ru–O shells were coupled to yield a sum of 2.  $2\sigma^2$  of the Ru–O bonds were also fixed at a physically reasonable value in the simulations. <sup>c</sup>  $R_F$  is the error sum calculated over reduced distances of Fourier transforms of 1–3 Å.

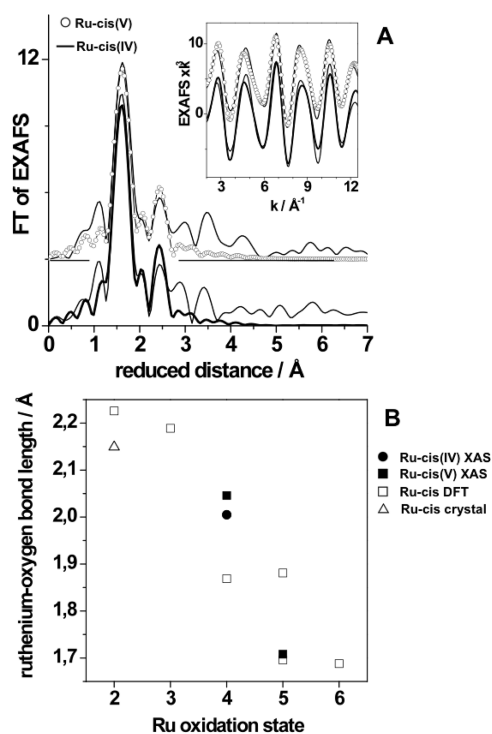


**Figure 5.** (A) Fourier transforms (FTs) of EXAFS spectra of complexes *cis*-[Ru<sup>IV</sup>(OH)<sub>2</sub>]<sup>2+</sup> and *cis*-[Ru<sup>V</sup>(OH)(O)]<sup>2+</sup>. FTs were calculated for  $k$ -values of 2–12.5 Å<sup>-1</sup> and using cos<sup>2</sup> windows extending over 10% at both  $k$ -range ends. Inset: Fourier-filtered EXAFS data corresponding to back transforms of FT spectra in a range of 1–3 Å of reduced distance. Solid lines and open circles correspond to simulations with parameters that are presented in Table 3 (fits a and d); thin black lines correspond to the experimental spectra. FT and  $k$ -space spectra are vertically displaced for comparison. (B) Ruthenium–oxygen bond lengths versus the ruthenium oxidation state from XAS, DFT, and X-ray crystallography. Data from X-ray and DFT is taken from Table 1, whereas data from XAS is in Table 3.

efficient geometry optimization, but inclusion of HF exchange in the M06-2X functional is expected to provide much more accurate electronic excitation energies.<sup>41</sup> Indeed, for *cis*-[Ru<sup>II</sup>(H<sub>2</sub>O)<sub>2</sub>]<sup>2+</sup>, the M06-2X//M06-L level predicts the first vertically excited singlet state  $S_1$  to be 58.8 kcal/mol above  $S_0$ ; the corresponding wavelength of 486 nm is in essentially quantitative agreement with the experimentally observed value of 490 nm. Geometric relaxation stabilizes this state by about 19.5 kcal/mol, but we find that a key factor in the isomerization reaction must be

**Table 4.** Aqueous 298 K Free Energies (kcal/mol) for Species Involved in the *cis*-[Ru<sup>II</sup>(H<sub>2</sub>O)<sub>2</sub>]<sup>2+</sup> to *trans*-[Ru<sup>II</sup>(H<sub>2</sub>O)<sub>2</sub>]<sup>2+</sup> Photoisomerization Reaction<sup>a</sup>

complex <sup>b</sup>	elec. state <sup>c</sup>	$G_{298K}^{\circ}$ (M06-2X)
<i>cis</i> -[Ru <sup>II</sup> (H <sub>2</sub> O) <sub>2</sub> ] <sup>2+</sup> (C- $S_0$ )	$S_0/S_1/T_1$	0.0/58.8/53.6
<i>cis</i> -[Ru <sup>II</sup> (H <sub>2</sub> O) <sub>2</sub> ] <sup>2+</sup> (C- $S_1$ )	$S_1/S_0$	39.3/41.0 <sup>d</sup>
<i>cis</i> -[Ru <sup>II</sup> (H <sub>2</sub> O)] <sup>2+</sup> (c- $S_0$ )	$S_0/S_1$	12.4/53.4
<i>cis</i> -[Ru <sup>II</sup> (H <sub>2</sub> O)] <sup>2+</sup> (c- $T_1$ )	$T_1$	27.1
TS-[Ru <sup>II</sup> (H <sub>2</sub> O)] <sup>2+</sup> (TS- $T_1$ )	$T_1$	29.0
<i>trans</i> -[Ru <sup>II</sup> (H <sub>2</sub> O)] <sup>2+</sup> (t- $T_1$ )	$T_1$	25.2
<i>trans</i> -[Ru <sup>II</sup> (H <sub>2</sub> O)] <sup>2+</sup> (t- $S_0$ )	$S_0/S_1$	27.6/43.9
<i>trans</i> -[Ru <sup>II</sup> (H <sub>2</sub> O)] <sup>2+</sup> (T- $S_0$ )	$S_0/S_1$	10.7/56.4
<i>trans</i> -[Ru <sup>II</sup> (H <sub>2</sub> O)] <sup>2+</sup> (T- $S_1$ )	$S_1/S_0$	36.4/36.1 <sup>d</sup>

<sup>a</sup> M06-2X//M06-L (lowest energy singlet and triplet states) and TD M06-2X//TD M06-L (excited singlet states) energies reported relative to optimized, ground-state *cis*-[Ru<sup>II</sup>(H<sub>2</sub>O)<sub>2</sub>]<sup>2+</sup>. Energies for mono-aqua complexes include accounting for an aqueous water molecule to preserve stoichiometry. <sup>b</sup> Abbreviations corresponding to those used in Figure 6 are listed. <sup>c</sup> The first spin state corresponds to that for which the geometry was optimized. The other states correspond to vertical excitations. <sup>d</sup> Excited states reoptimized with TD M06-2X.

intersystem crossing to the triplet  $T_1$  state, which is lower than the  $S_1$  state by about 5 kcal/mol at the  $S_0$  geometry. Unlike the  $S_0$  and  $S_1$  states, the  $T_1$  state spontaneously dissociates one aquo ligand to generate a mono-aqua complex, *cis*-[Ru<sup>II</sup>(H<sub>2</sub>O)]<sup>2+</sup>, that has a coordination number of 5 but maintains a pseudo-octahedral geometry with the vacant site *cis* to the remaining aqua ligand. The relaxed triplet state is sufficiently far above the corresponding mono-aqua  $S_0$  state in energy that decay may be expected to be slow. As an alternative to decay, ligand rearrangement can take place to move the vacant site so as to generate *trans*-[Ru<sup>II</sup>(H<sub>2</sub>O)]<sup>2+</sup>, also in a pseudo-octahedral geometry. On the  $T_1$  potential energy surface, a transition-state structure for this process is found having a free energy of activation of 1.9 kcal/mol and the product t- $T_1$  is predicted to be 1.9 kcal/mol lower in energy than its *cis* counterpart.

Interestingly, the *trans* t- $S_0$  state is much higher in energy than the *cis* c- $S_0$  state (see Table 4), so that thermally activated intersystem crossing from t- $T_1$  to t- $S_0$  may take place (the nomenclature used here is as follows: c and C refer to the *cis* di- and mono-aqua complexes respectively; the same analogy is used for the *trans* case; see Table 4 and Figure 6). On the *trans* singlet surface, recoordination of the second aquo ligand to generate the final *trans*-[Ru<sup>II</sup>(H<sub>2</sub>O)<sub>2</sub>]<sup>2+</sup> complex is predicted to



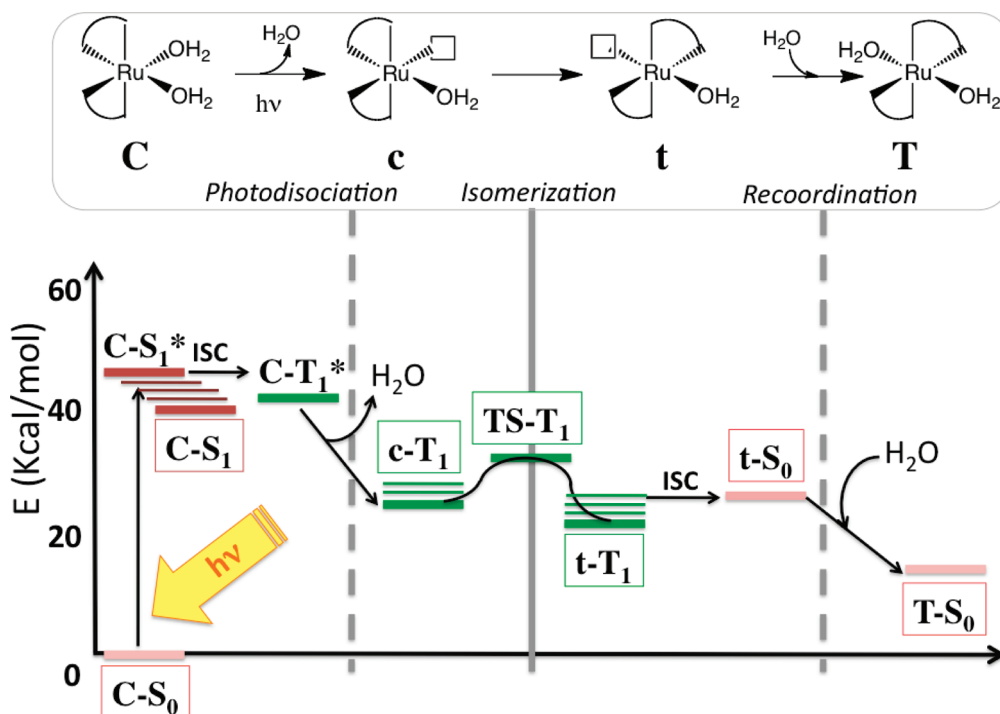


**Figure 6.** Energy diagram (TD M06-2X//M06-L; energies not perfectly to scale to improve clarity) for the photoisomerization process. Upper- and lower-case letters refer to di- and monoaqua complexes, respectively, both *cis* (C,c) and *trans* (T,t). A box around a compound name indicates a state for which the geometry was optimized; unboxed state-energy levels deriving from C-S<sub>0</sub> correspond to vertical energy calculations at the S<sub>0</sub> geometry. In the scheme at top, a vacant coordination site is indicated by an open box.

be spontaneous. The driving force for photoisomerization thus appears to be the greater stability of the *trans* triplet state of monoaquo  $[\text{Ru}^{\text{II}}(\text{H}_2\text{O})]^{2+}$  together with an efficient pathway to regenerate the *trans* singlet state of diaquo  $[\text{Ru}^{\text{II}}(\text{H}_2\text{O})_2]^{2+}$ .

#### 4. CONCLUSIONS

The electronic structures of *cis*- and *trans*- $[\text{Ru}^{\text{II}}(\text{H}_2\text{O})_2]^{2+}$  and more highly oxidized species derived from these complexes have been studied by means of UV–vis, EPR, and XAS spectroscopies together with DFT calculations. EPR and DFT indicate that in almost all cases lowest spin configurations are favored, and in particular, *cis*- $[\text{Ru}^{\text{IV}}(\text{OH})_2]^{2+}$  and *cis*- $[\text{Ru}^{\text{V}}(\text{O})(\text{OH})]^{2+}$  have singlet and doublet ground states, respectively. XAS and DFT analyses of these same more highly oxidized complexes indicate a decrease of Ru–O bond distances with increasing oxidation together with an enhancement of the multiple bonding character of the O–Ru–O unit, although they also indicate that substantial oxidation takes place at O, as opposed to Ru, by the time the formal  $\text{Ru}^{\text{V}}$  state is reached. Last, DFT predicts the photochemical isomerization of *cis*- $[\text{Ru}^{\text{II}}(\text{H}_2\text{O})_2]^{2+}$  to *trans*- $[\text{Ru}^{\text{II}}(\text{H}_2\text{O})_2]^{2+}$  to proceed via dissociation of an aqua ligand, which is predicted to be labile on the triplet-state potential energy surface that can be reached through intersystem crossing, followed by rearrangement and recoordination of water upon crossing back to the ground-state singlet surface.

#### ■ ASSOCIATED CONTENT

**Supporting Information.** Orbitals, energies, and optimized structures for all the studied species. This material is available free of charge via the Internet at <http://pubs.acs.org>.

#### ■ AUTHOR INFORMATION

##### Corresponding Author

\*E-mail: [gagliard@umn.edu](mailto:gagliard@umn.edu), [cramer@umn.edu](mailto:cramer@umn.edu), [allobet@iciq.es](mailto:allobet@iciq.es).

#### ■ ACKNOWLEDGMENT

Support from SOLAR-H2 (EU 212508), MICINN (CTQ2010-21497 and Consolider Ingenio CSD2006-0003), and the Generalitat de Catalunya (CIRIT/2009 SGR 69) are gratefully acknowledged. N.P. is grateful for an MICINN doctoral grant. M.H. thanks the Deutsche Forschungsgemeinschaft for a Heisenberg-Fellowship and for funding (grant Ha3265/3-1). We thank Dr. Maarten Nachtegaal at the SuperXAS beamline of SLS for excellent technical support. C.J.C. thanks the U.S. National Science Foundation (CHE09-52054). The Swedish Energy Agency and The K&A Wallenberg Foundation also thanked for financial support.

#### ■ REFERENCES

- (1) (a) Lappin, A. G.; Marusak, R. A. *Coord. Chem. Rev.* **1991**, 109, 125–180. (b) Griffith, W. P. *Chem. Soc. Rev.* **1992**, 21, 179–185. (c) Wing-Sze Hui, J.; Wong, W.-T. *Coord. Chem. Rev.* **1998**, 172, 389–436. (d) Clarke, M. J. *Coord. Chem. Rev.* **2002**, 232, 69–93. (e) Meyer, T. J.; Huynh, M. H. V. *Inorg. Chem.* **2003**, 42, 8140–8169.
- (2) (a) Balzani, V.; Juris, A. *Coord. Chem. Rev.* **2001**, 211, 97–115. (b) Coudret, C.; Balzani, V.; Barigelletti, F.; De Cola, L.; Fannigni, L. *Chem. Rev.* **1994**, 94, 993–1019. (c) Meyer, T. J. *Acc. Chem. Res.* **1989**, 22, 163.
- (3) (a) Kelley, S. O.; Barton, J. K. *Science* **1999**, 238, 375. (b) Hall, D. B.; Holmlin, R. E.; Barton, J. K. *Nature* **1996**, 384, 731. (c) Burrows, C. J.; Muller, J. G. *Chem. Rev.* **1998**, 98, 1109. (d) Weatherly, S. C.; Yang, I. V.; Thorp, H. H. *J. Am. Chem. Soc.* **2001**, 123, 1236.



- (4) (a) Murahashi, S. I.; Takaya, H.; Naota, T. *Pure Appl. Chem.* **2002**, *74*, 19–24. (b) Naota, T.; Takaya, H.; Murahashi, S.-I. *Chem. Rev.* **1998**, *98*, 2599–2660. (c) Rodríguez, M.; Romero, I.; Llobet, A.; Deronzier, A.; Biner, M.; Parella, T.; Stoeckli-Evans, H. *Inorg. Chem.* **2001**, *40*, 4150–4156. (d) Jauregui-Haza, U. J.; Dessoudeix, M.; Kalk, Ph.; Wilhelm, A. M.; Delmas, H. *Catal. Today* **2001**, *66*, 297–302.
- (5) Benniston, A. C.; Harriman, A. *Mater. Today* **2008**, *11*, 26–34.
- (6) (a) Sala, X.; Rodríguez, M.; Romero, I.; Escriche, L.; Llobet, A. *Angew. Chem., Int. Ed.* **2009**, *48*, 2842. (b) Romain, S.; Vigara, L.; Llobet, A. *Acc. Chem. Res.* **2009**, *42*, 1944–1953. (c) Sartorel, A.; Carraro, M.; Scorrano, G.; De Zorzi, R.; Geremia, S.; McDaniel, N. D.; Bernhard, S.; Bonchio, M. *J. Am. Chem. Soc.* **2008**, *130*, 5006. (d) Puntoriero, F.; La Ganga, G.; Sartorel, A.; Carraro, M.; Scorrano, G.; Bonchio, M.; Campagna, S. *Chem. Commun.* **2010**, *46*, 4725–4727. (e) Geletii, Y. V.; Botar, B.; Koegler, P.; Hillesheim, D. A.; Musaev, D. G.; Hill, C. L. *Angew. Chem., Int. Ed.* **2008**, *47*, 3896–3899. (f) Geletii, Y. V.; Huang, Z.; Hou, Y.; Musaev, D. G.; Lian, T.; Hill, C. L. *J. Am. Chem. Soc.* **2009**, *131*, 7522–7523.
- (7) (a) Chen, Z.; Concepcion, J. J.; Luo, H.; Hull, J. F.; Paul, A.; Meyer, T. J. *J. Am. Chem. Soc.* **2010**, *132*, 17670–17673. (b) Concepcion, J.; Jurss, J. W.; Templeton, J. L.; Meyer, T. J. *J. Am. Chem. Soc.* **2008**, *130*, 16462–16463. (c) Zhang, G.; Zong, R.; Tseng, H. W.; Thummel, R. P. *Inorg. Chem.* **2008**, *47*, 990–998.
- (8) (a) Wasylenko, D. J.; Ganesamoorthy, C.; Henderson, M. A.; Berlinguette, C. P. *Inorg. Chem.* **2011**, *50*, 3662–3672. (b) Wasylenko, D. J.; Ganesamoorthy, C.; Henderson, M. A.; Koivisto, B. D.; Osthoff, H. D.; Berlinguette, C. P. *J. Am. Chem. Soc.* **2010**, *132*, 16094–16106. (c) Duan, L.; Xu, Y.; Zhang, P.; Wang, M.; Sun, L. *Inorg. Chem.* **2010**, *49*, 209–215. (d) Duan, L.; Fischer, A.; Xu, Y.; Sun, L. *J. Am. Chem. Soc.* **2009**, *131*, 10397–10399. (e) Yoshida, M.; Masaoka, S.; Abe, J.; Sakai, K. *Chem. Asian J.* **2010**, *5*, 2369–2378.
- (9) (a) Bozoglian, F.; Romain, S.; Ertem, M. Z.; Todorova, T. K.; Sens, C.; Mola, J.; Rodríguez, M.; Romero, I.; Benet-Buchholz, J.; Fontrodona, X.; Cramer, C. J.; Gagliardi, L.; Llobet, A. *J. Am. Chem. Soc.* **2009**, *131*, 15176–15187. (b) Sartorel, A.; Miró, P.; Salvadori, E.; Romain, S.; Carraro, M.; Scorrano, G.; Di Valentin, M.; Llobet, A.; Bo, C.; Bonchio, M. *J. Am. Chem. Soc.* **2009**, *131*, 1651–1653. (c) Mola, J.; Mas-Marza, E.; Sala, X.; Romero, I.; Rodríguez, M.; Vinas, C.; Parella, T.; Llobet, A. *Angew. Chem., Int. Ed.* **2008**, *47*, 5830–5832. (d) Yamada, H.; Hurst, J. K. *J. Am. Chem. Soc.* **2000**, *122*, 5303–5311.
- (10) See, for instance: Murray, K. S. *Adv. Inorg. Chem.* **1995**, *43*, 261–358.
- (11) (a) Sala, X.; Ertem, M. Z.; Vigara, L.; Todorova, T. K.; Chen, W.; Rocha, R. C.; Cramer, C. J.; Gagliardi, L.; Llobet, A. *Angew. Chem., Int. Ed.* **2010**, *49*, 7745–7747. (b) Dobson, J. C.; Meyer, T. J. *Inorg. Chem.* **1988**, *27*, 3283–3291.
- (12) Cramer, C. J. *Essentials of Computational Chemistry: Theories and Models*; John Wiley & Sons: Chichester, U. K., 2004.
- (13) Runge, E.; Gross, E. K. U. *Phys. Rev. Lett.* **1984**, *52*, 997–1000.
- (14) Johnson, E. C.; Sullivan, B. P.; Salmon, D. J.; Adeyemi, S. A.; Meyer, T. J. *Inorg. Chem.* **1978**, *17*, 2211–2215.
- (15) Dau, H.; Liebisch, P.; Haumann, M. *Anal. Bioanal. Chem.* **2003**, *376*, 562–583.
- (16) Zabinsky, S. I.; Rehr, J. J.; Ankudinov, A. L.; Albers, R. C.; Eller, M. J. *Phys. Rev. B* **1995**, *52*, 2995–3009.
- (17) Zhao, Y.; Truhlar, D. G. *J. Chem. Phys.* **2006**, *125*, 194101.
- (18) Zhao, Y.; Truhlar, D. G. *MN-GFM*, version 4.1; University of Minnesota: Minneapolis, MN, 2008.
- (19) Frisch et al. *Gaussian 03*, revision D.01; Gaussian, Inc.: Wallingford, CT, 2004.
- (20) Dolg, M.; Wedig, U.; Stoll, H.; Preuss, H. *J. Chem. Phys.* **1987**, *86*, 866.
- (21) Hehre, W. J.; Radom, L.; Schleyer, P. V. R.; Pople, J. A. *Ab Initio Molecular Orbital Theory*; Wiley: New York, 1986.
- (22) (a) Ziegler, T.; Rauk, A.; Baerends, E. J. *Theor. Chim. Acta* **1977**, *43*, 261. (b) Noodleman, L.; Norman, J. G. *J. Chem. Phys.* **1979**, *70*, 4903. (c) Yamaguchi, K.; Jensen, F.; Dorigo, A.; Houk, K. N. *Chem. Phys. Lett.* **1988**, *149*, 537. (d) Noodleman, L.; Case, D. A. *Adv. Inorg. Chem.* **1992**, *38*, 423. (e) Lim, M. H.; Worthington, S. E.; Dulles, F. J.; Cramer, C. J. *Chemical Applications of Density Functional Theory*; Laird, B. B., Ross, R. B., Ziegler, T., Eds.; American Chemical Society: Washington, DC, 1996; Vol. 629, p 402. (f) Isobe, H.; Takano, Y.; Kitagawa, Y.; Kawakami, T.; Yamanaka, S.; Yamaguchi, K.; Houk, K. N. *Mol. Phys.* **2002**, *100*, 717.
- (23) Marenich, A. V.; Cramer, C. J.; Truhlar, D. G. *J. Phys. Chem. B* **2009**, *113*, 6378.
- (24) (a) Ben-Naim, A. *Statistical Thermodynamics for Chemists and Biochemists*; Plenum: New York, 1992. (b) Kelly, C. P.; Cramer, C. J.; Truhlar, D. G. *J. Phys. Chem. A* **2006**, *110*, 2493–2499. (c) Kelly, C. P.; Cramer, C. J.; Truhlar, D. G. *J. Phys. Chem. B* **2006**, *110*, 16066–16081. (d) Bryantsev, V. S.; Diallo, M. S.; Goddard, W. A. *J. Phys. Chem. B* **2008**, *112*, 9709–9719.
- (25) Frisch et al. *Gaussian 09*, revision A.02; Gaussian, Inc.: Wallingford, CT, 2010.
- (26) Zhao, Y.; Truhlar, D. G. *Acc. Chem. Res.* **2008**, *41*, 215–241.
- (27) (a) Roos, B. O.; Taylor, P. R. *Chem. Phys.* **1980**, *48* (2), 157–173. (b) Andersson, K.; Malmqvist, P. A.; Roos, B. O.; Sadlej, A. J.; Wolinski, K. *J. Phys. Chem.* **1990**, *94* (14), 5483–5488. (c) Andersson, K.; Malmqvist, P. A.; Roos, B. O. *J. Chem. Phys.* **1992**, *96* (2), 1218–1226.
- (28) Aquilante, F.; De Vico, L.; Ferre, N.; Ghigo, G.; Malmqvist, P. A.; Neogrady, P.; Pedersen, T. B.; Pitonak, M.; Reiher, M.; Roos, B. O.; Serrano-Andres, L.; Urban, M.; Veryazov, V.; Lindh, R. *Comput. Chem.* **2010**, *31*, 224–247.
- (29) Hess, B. A. *Phys. Rev. A* **1986**, *33*, 3742.
- (30) Roos, B. O.; Lindh, R.; Malmqvist, P.-Å.; Veryazov, V.; Widmark, P.-O. *J. Phys. Chem. A* **2005**, *109*, 6575.
- (31) Welch, T. W.; Ciftan, S. A.; White, P. S.; Thorp, H. H. *Inorg. Chem.* **1997**, *36*, 4812–4821.
- (32) Che, C.-M.; Lai, T.-F.; Wong, K.-Y. *Inorg. Chem.* **1987**, *26*, 2289–2299.
- (33) Perrier, S.; Lau, T. C.; Kochi, J. K. *Inorg. Chem.* **1990**, *29*, 4190–4195.
- (34) Jude, H.; White, P. S.; Dattelbaum, D. M.; Rocha, R. C. *Acta Crystallogr., Sect. E* **2008**, *E64*, [Online].
- (35) Gama Sauaia, M.; Founi, E.; de Almeida Santos, H.; Do Prado Gambardella, M. T.; Del Lama, M. P. F. M.; Fernando Guimeraes, L.; Santana da Silva, R. *Inorg. Chem. Commun.* **2003**, *6*, 864–868.
- (36) Durham, B.; Wilson, S. R.; Hodgson, D. J.; Meyer, T. J. *J. Am. Chem. Soc.* **1980**, *102*, 600–607.
- (37) (a) Chatt, J.; Leigh, G. J.; Mingos, D. M. P. *J. Chem. Soc. A* **1969**, 1674. (b) DeSimone, R. E. *J. Am. Chem. Soc.* **1973**, *95*, 623.
- (38) Dengel, A. C.; Griffith, W. P. *Inorg. Chem.* **1991**, *30*, 869–871.
- (39) (a) Okamoto, K.; Miyawaki, J.; Nagai, K.; Matsumura, D.; Nojima, A.; Yokoyama, T.; Kondoh, H.; Ohta, T. *Inorg. Chem.* **2003**, *42*, 8682–8689. (b) Valli, M.; Miyata, S.; Wakita, H.; Yamaguchi, T.; Kikuchi, A.; Umakoshi, K.; Imamura, T.; Sasaki, Y. *Inorg. Chem.* **1997**, *36*, 4622–4626. (c) Sikora, M.; Oates, C. J.; Szczerba, W.; Kapusta, C.; Zukrowski, J.; Zajac, D.; Borowiec, A.; Ruiz-Bustos, R.; Battle, P. D.; Rosseinsky, M. J. *Alloys Compd.* **2007**, *442*, 265–267. (d) Artero, V.; Proust, A.; Herson, P.; Villain, F.; Moulin, C. C. D.; Gouzerh, P. *J. Am. Chem. Soc.* **2003**, *125*, 11156–11157. (e) Lahootun, V.; Besson, C.; Villanneau, R.; Villain, F.; Chamoiseau, L. M.; Boubekeur, K.; Blanchard, S.; Thouvenot, R.; Proust, A. *J. Am. Chem. Soc.* **2007**, *129*, 7127–7135.
- (40) (a) Dau, H.; Liebisch, P.; Haumann, M. *Phys. Scr.* **2005**, *T115*, 844–846. (b) Haumann, M.; Müller, C.; Liebisch, P.; Iuzzolino, L.; Dittmer, J.; Grabolle, M.; Neisius, T.; Meyer-Klaucke, W.; Dau, H. *Biochemistry* **2005**, *44*, 1894–1908. (c) Havelius, K. G.; Reschke, S.; Horn, S.; Doring, A.; Niks, D.; Hille, R.; Schulzke, C.; Leimkuhler, S.; Haumann, M. *Inorg. Chem.* **2011**, *50*, 741–748.
- (41) (a) Dreuw, A.; Head-Gordon, M. *Chem. Rev.* **2005**, *105*, 4009–4037. (b) Jacquemin, D.; Perpète, E. A.; Ciofini, I.; Adamo, C. *J. Chem. Theory Comput.* **2010**, *6*, 1532–1537.